https://doi.org/10.5194/egusphere-2026-5021
Preprint. Discussion started: 25 August 2026

Online zero-Doppler reference tracking and wind speed correction for an iodine-cell Rayleigh Doppler lidar: method and validation

Zhiqiang Tan[1,2], Shijiang Shu[3], Lingbing Bu[1,2], Bin Yang[1,7], Cong Huang[4,5,6], Yungang Wang[4,5,6], Cong Wang[4,5,6]

[1]State Key Laboratory of Environment Characteristics and Effects for Near-space, Nanjing University of Information Science and Technology, Nanjing, 210044, China
[2]Key Laboratory of Intelligent Support Technology for Complex Environments, Ministry of Education, Nanjing University of Information Science and Technology, Nanjing, 210044, China
[3]HuaYun METSTAR Radar (Beijing) Company, Limited, Beijing, 100094, China
[4]National Satellite Meteorological Center (National Centre for Space Weather), Beijing, 100081, China
[5]Innovation Center for FengYun Meteorological Satellite (FYSIC), Beijing, 100081, China
[6]Key Laboratory of Space Weather, CMA, Beijing, 100081, China
[7]Nanjing Movelaser Company, Limited, Nanjing, 210034, China

Correspondence to: Lingbing Bu (lingbingbu@nuist.edu.cn)

Abstract.

In an iodine-cell-based Rayleigh Doppler lidar (RDLD), slow drift in the relative spectral position between the transmitted laser frequency and the discriminator response can shift the zero-Doppler reference and introduce systematic wind errors. This study proposes and validates an online zero-Doppler reference tracking and wind correction method based on time-division multiplexed measurements of seed reference light. The seed reference light and atmospheric backscatter share a single iodine-cell frequency discriminator, and the seed transmittance is used to determine the spectral position of the emitted laser relative to the current discriminator response and update the zero-Doppler reference online. In a dynamic frequency-tracking experiment, the difference between Doppler frequency-discrimination receiver (DFDR) and wavemeter measurements had a standard deviation of 1.25 MHz. During the 8 h continuous measurement, hour-scale variations of several megahertz were observed in the relative spectral position, indicating that the zero-Doppler reference may not remain strictly constant during long-term operation. With integration times of 100–1000 s, the Allan deviation of the frequency measurements was reduced to approximately 0.29 MHz. The frequency difference between the seed reference light and pulsed laser had a standard deviation of 1.14 MHz, supporting the use of the seed reference light to track pulsed-laser frequency variations. In atmospheric observations, the mean vertical wind speed shifted from approximately 1.2 to −0.34 m s^{-1} after zero-Doppler reference correction. In a controlled frequency-offset experiment, RDLD retrieved equivalent wind speeds agreed well with values derived from independent wavemeter measurements. Measured zonal and meridional winds also agreed well with ERA5 reanalysis in their major vertical structures and temporal evolution. These results demonstrate that the method enables online monitoring and correction of the RDLD zero-Doppler reference without continuous reliance on an external wavemeter, improving the stability of long-term wind measurements.

https://doi.org/10.5194/egusphere-2026-5021
Preprint. Discussion started: 25 August 2026

1 Introduction

The stratosphere and mesosphere are key regions for atmospheric coupling, where accurate temperature and wind measurements are important for studies of global circulation, wave–mean-flow interactions, and space-weather responses (Holton et al., 2013). Rayleigh Doppler lidar (RDLD) measures stratospheric and mesospheric temperature and wind using Rayleigh backscatter generated through the interaction of laser light with atmospheric molecules. It provides direct observations with high temporal and spatial resolution at altitudes in the stratosphere and mesosphere that are difficult to cover routinely with radiosondes, and offers complementary altitude coverage to other observational techniques, including sodium resonance fluorescence lidar, Mesosphere–Stratosphere–Troposphere (MST) radar, and medium-frequency (MF) radar (Donfrancesco et al., 1996; Keckhut et al., 2001; Tsutsumi and Aso, 2005; Baumgarten et al., 2010; Li et al., 2012; Qiao et al., 2020). At present, only a few RDLD systems are capable of long-term stable operation, including the ALOMAR Rayleigh/Mie/Raman (RMR) lidar and the OHP Doppler Rayleigh lidar (Khaykin et al., 2020; Fiedler et al., 2024). Their long-term observations have supported studies of gravity waves, atmospheric tides, and planetary waves (Baumgarten et al., 2015; Khaykin et al., 2015; Strelnikova et al., 2021;Liu et al., 2022; Mossad et al., 2025).

RDLD wind retrieval uses an optical frequency discriminator to convert the Doppler shift of atmospheric backscatter into a measurable transmittance change, which is mapped back to frequency using the calibrated frequency–transmittance response (Liu et al., 2002; Liu et al., 2007). The spectral position of the transmitted laser on this response curve defines the zero-Doppler reference. At 532 nm, a 1 m s^{-1} line-of-sight (LOS) wind change corresponds to a Doppler shift of approximately 3.75 MHz, so megahertz-scale reference shifts can produce noticeable wind biases. During long-term operation, environmental and instrumental changes may alter either the laser frequency or discriminator response, but both lead to changes in their relative spectral position. If this variation is not tracked or the zero-Doppler reference is treated as fixed, time-dependent systematic biases may affect the consistency of long-term wind observations.

Existing RDLD systems generally maintain Doppler wind accuracy by stabilizing the laser and frequency discriminator and by independently monitoring transmitted-laser frequency deviations. For example, the ALOMAR RMR lidar locks the seed laser to the iodine 1109 absorption line and uses seed injection to control two Q-switched Nd:YAG lasers (Zahn et al., 2000). The iodine-cell temperature is stabilized, and periodic spectral scans are performed to verify the long-term stability of its transmittance spectrum (Baumgarten, 2010). Because seed injection can introduce megahertz-scale offsets between the seed and pulsed lasers, the ALOMAR RMR lidar uses independent I_2 and FPI spectrometers to monitor their frequency difference in real time (Fiedler et al., 2024; Fiedler et al., 2026). Its Doppler Rayleigh Iodine Spectrometer also measure a stable seed reference light after each laser pulse to track relative detection-efficiency changes between the reference and iodine-cell channels and correct system-response differences (Hildebrand, 2014). Similarly, Yan et al. (2017) used a separate iodine cell to monitor seed-injection status and reject echoes from pulses with failed injection.

These above studies have improved the reliability of emitted-laser frequency control, but most approaches still stabilize or monitor the laser and discriminator separately. As a result, the relative spectral position between the laser frequency used for

https://doi.org/10.5194/egusphere-2026-5021
Preprint. Discussion started: 25 August 2026

wind retrieval and the discriminator response must be determined indirectly from multiple independently measured quantities. If this position could instead be measured online through the same frequency-discrimination optical path, the zero-Doppler reference could be tracked more directly with less reliance on independent parameters.

Our team deployed an iodine-cell-based RDLD in Jiuquan, Gansu, China (98.5° E, 39.8° N), for measurements of atmospheric temperature and wind at altitudes of 30–70 km. The system uses two independent iodine absorption cells, one for laser frequency locking and the other for Doppler frequency discrimination of atmospheric backscatter. Because the temperatures and iodine-vapor conditions of the two cells cannot be maintained identically at all times, their transmittance spectra may exhibit time-varying relative differences. Therefore, even when the seed laser is locked to the spectral edge of the locking cell, its spectral position on the frequency–transmittance response curve of the DFDR iodine cell may not remain constant. Consequently, the zero-Doppler reference of the system may still drift over time. The system employs an all-solid-state laser based on a master oscillator power amplifier (MOPA) architecture. The seed laser is successively amplified by multiple end-pumped amplifier stages and a slab power amplifier to generate high-energy laser pulses (Wang J. et al., 2010; Li S. et al., 2013). Unlike conventional injection-seeded Q-switched lasers, this architecture avoids issues such as loss of injection locking, longitudinal-mode competition, and multimode oscillation, allowing the frequency of the output laser pulses to be primarily determined by the seed laser frequency. This provides the basis for using the seed laser frequency as a reference for the pulsed-laser frequency. The frequency consistency between the seed reference light and the pulsed laser is further validated in a subsequent experiment.

Building on this design, this study proposes a method for online tracking of the zero-Doppler reference and wind correction. The method focuses on the relative spectral position between the transmitted laser and the actual Doppler frequency-discrimination response, treating the zero-Doppler reference as an observable and updatable system state rather than a fixed parameter determined by prior calibration. Specifically, within each measurement cycle, the DFDR sequentially measures the seed reference light and atmospheric backscatter. The measured transmittance of the seed reference light through the iodine cell is then used to determine online the zero-Doppler reference position of the transmitted laser on the current frequency–transmittance response curve of the discriminator. The resulting variation in the zero-Doppler reference is directly used to correct biases in the retrieved Doppler shift of atmospheric backscatter caused by relative changes in the transmitted laser frequency or the discriminator response.

The proposed method is validated through laboratory tests and atmospheric observations. The proposed method is validated through laboratory tests and atmospheric observations. First, the frequency–transmittance response of the DFDR iodine cell is calibrated, and experiments with a freely drifting seed laser and an 8 h continuous measurement are conducted to evaluate the dynamic frequency-tracking capability of the DFDR and its long-term performance in tracking the zero-Doppler reference. Second, the frequency consistency between the seed reference light and the pulsed laser is verified through simultaneous frequency measurements. The effectiveness of the zero-Doppler reference correction and the performance of wind retrieval are then evaluated using vertical atmospheric observations and controlled frequency-offset experiments. Finally, the horizontal

https://doi.org/10.5194/egusphere-2026-5021
Preprint. Discussion started: 25 August 2026

winds obtained from continuous nighttime observations are compared with ERA5 reanalysis to assess the system performance in atmospheric wind measurements.

The remainder of this paper is organized as follows. Section 2 presents an overview of the RDLD system and the optomechanical configuration for online zero-Doppler reference measurement. Section 3 describes the principles of zero-Doppler reference tracking and wind correction. Section 4 presents the validation experiments and their results. Section 5 summarizes the main conclusions.

2 Instrument and measurement configuration

2.1 Instrument overview

As seen in Fig. 1, the RDLD is equipped with three telescopes pointing vertically (VT), westward at an inclined angle (WT), and northward at an inclined angle (NT), respectively. The VT channel is used to measure atmospheric temperature and vertical wind, while the WT and NT channels measure zonal and meridional winds, respectively. The system employs a MOPA all-solid-state laser and a time-division multiplexing laser beam-splitting assembly (TDM-LBS) to switch sequentially among the three observation channels according to a predefined timing sequence. The pulsed laser is directed to a reflector mounted on the side of the corresponding telescope and then transmitted into the atmosphere along the respective line of sight. The signal integration times are 5 min for the VT channel and 12.5 min for each of the two inclined channels. The three channels are operated sequentially in the order VT, WT, and NT to complete one measurement cycle, yielding a set of atmospheric temperature, zonal-wind, and meridional-wind profiles. A detailed description of the system configuration and measurement performance can be found in our previous work (Yang et al., 2025).

https://doi.org/10.5194/egusphere-2026-5021
Preprint. Discussion started: 25 August 2026

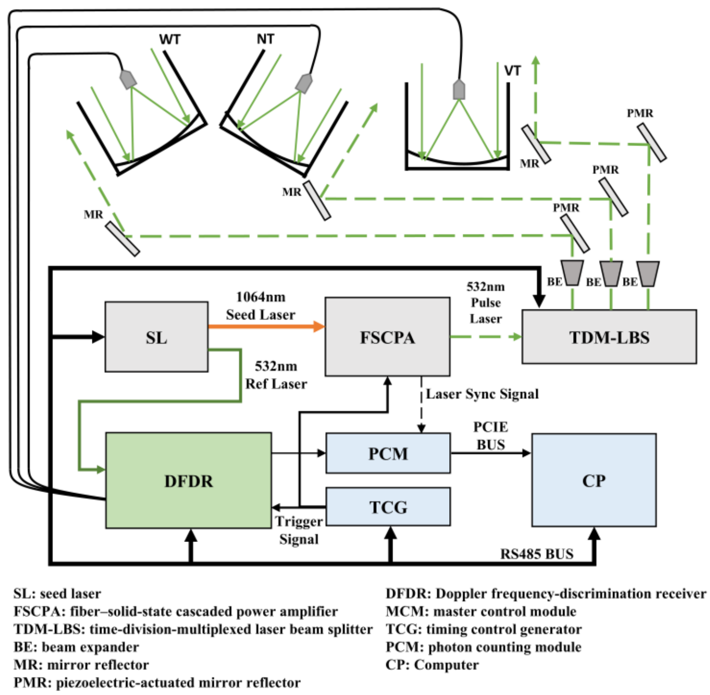

Figure 1: Schematic of the RDLD system. The RDLD control computer (CP) sends control commands to the functional modules and receives their operating-status information via an RS485 bus. The timing control generator (TCG) provides synchronized timing signals for laser triggering and chopper gating. The photon-counting module (PCM) acquires the photon-counting signals from the DFDR and transfers them to the CP for data processing. The green dashed lines indicate the optical paths of the 532 nm pulsed laser, and the green solid lines indicate the optical paths of the 532 nm seed reference light.

2.2 Receiver and channel time-division multiplexing

The DFDR is used for both atmospheric-backscatter Doppler-shift measurement and online tracking of the zero-Doppler reference. The DFDR configuration in Fig. 2 includes two fiber-optic input channels that receive atmospheric backscatter and seed reference light, hereafter referred to as the atmospheric-backscatter channel and the seed-reference channel, respectively. Each channel is equipped with a mechanical chopper. Under timing control, the two choppers are alternately opened, allowing the atmospheric backscatter and seed reference light to enter the same iodine-cell in separate time windows. In the frequency-discrimination optical path, the two photomultiplier tubes before and after the iodine cell are denoted by P_R and P_I, respectively. They measure the reference signal that before entering the iodine cell and the frequency-discriminated signal transmitted through the iodine cell, respectively.

https://doi.org/10.5194/egusphere-2026-5021
Preprint. Discussion started: 25 August 2026

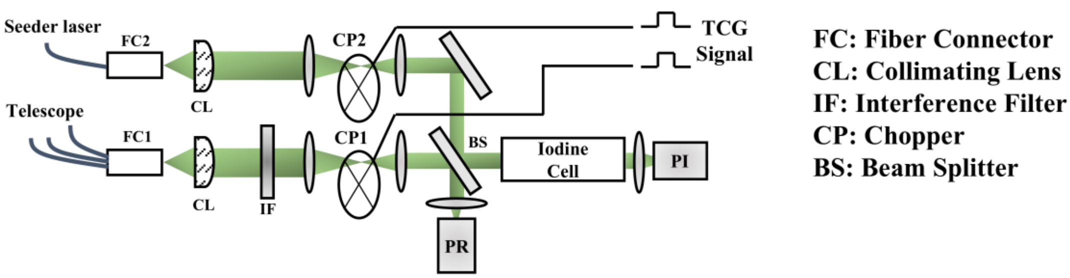

Figure 2: DFDR optical configuration

Figure 3 shows the timing control scheme, in which the timing control generator (TCG) generates the mechanical-chopper control signals and laser trigger signal based on a 600 Hz reference clock. The open-duty cycles of the choppers in the atmospheric-backscatter and seed-reference channels are 50% and 20%, respectively. The seed-reference channel is opened approximately 100 μs later than the atmospheric-backscatter channel. This timing allows the seed reference light to enter the frequency-discrimination optical path only after atmospheric-backscatter sampling is completed, avoiding temporal overlap between the two signals. The laser trigger signal is generated by dividing the 600 Hz reference clock by three, giving a repetition rate of 200 Hz, and the trigger delay is adjusted to control the starting altitude of atmospheric-backscatter detection. Under this timing configuration, the effective atmospheric-backscatter detection range is approximately 30–155 km, while the open time of the seed-reference channel corresponds to an equivalent range of approximately 30 km. During switching between the two choppers, there is a time window in which both choppers are closed. Both optical signals are blocked during this interval, allowing the photomultiplier-tube dark counts to be measured.

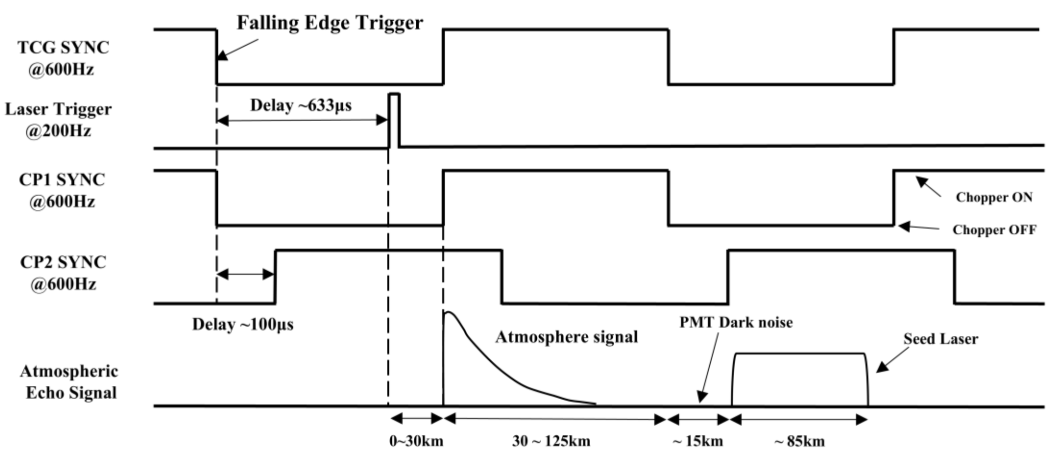

Figure 3: DFDR channel time-division multiplexing control sequence

Figure 4 shows a typical set of raw atmospheric-backscatter signal profiles. The integration time for each raw data point is 1 μs, corresponding to a minimum range resolution of 150 m. Owing to the timing control of the mechanical chopper, near-range atmospheric backscatter below 30 km is blocked, and the effective atmospheric-backscatter signal extends from approximately

https://doi.org/10.5194/egusphere-2026-5021
Preprint. Discussion started: 25 August 2026

30 to 140 km. The transmission window of the seed-reference channel corresponds to an equivalent range of approximately 200–240 km. The seed-reference transmittance used to determine the zero-Doppler reference is obtained from the signal ratio between the P_R and P_I channels within the seed-reference time window.

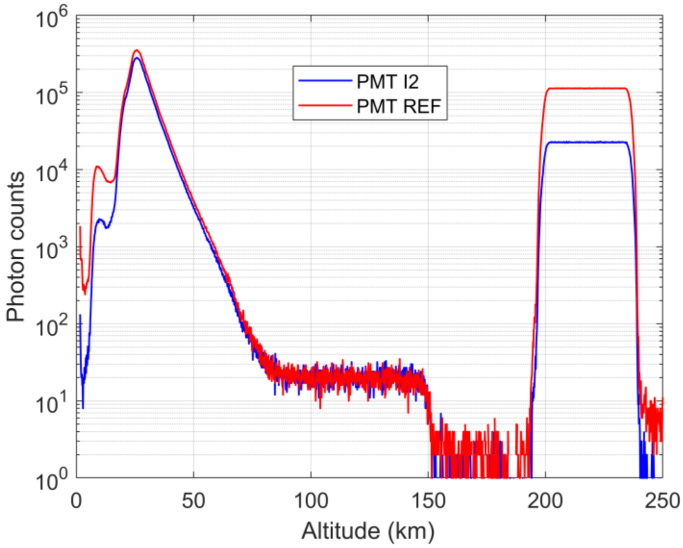

Figure 4: Raw atmospheric-backscatter signal profiles of the RDLD. The blue and red lines represent the DFDR iodine-cell and reference channels, respectively.

3 Theory and method

3.1 Doppler wind retrieval

Figure 5 illustrates the principle of Doppler frequency discrimination using the iodine 1109 absorption line in the RDLD. The theoretical frequency–transmittance response function F of the iodine-cell discriminator is obtained by convolving the measured iodine transmittance spectrum I with the Cabannes line $\mathfrak{R}$. The response is jointly determined by the transmitted laser frequency ν_0, the Doppler frequency shift of atmospheric backscatter $\Delta\nu$, and the atmospheric temperature T (Liu et al., 2002):

$$F(\nu_0 + \Delta\nu, T) = \int_{-\infty}^{\infty} I(\nu')\,\mathfrak{R}(\nu' - \nu_0 - \Delta\nu, T)\,d\nu' , \tag{1}$$

where $\Delta\nu_D(T)$ is the full width at half maximum (FWHM) of the Gaussian line shape. The atmospheric temperature is retrieved from the atmospheric-backscatter signals measured by the VT channel using the Chanin–Hauchecorne method, which is based on the assumptions of hydrostatic equilibrium and the ideal gas law (Hauchecorne and Chanin, 1980).

At altitudes above 30 km, the atmospheric pressure is sufficiently low that collisional broadening of the Cabannes line is negligible compared with Doppler broadening. The Cabannes linewidth is therefore dominated by Doppler broadening due to molecular thermal motion and can be approximated by a Gaussian line shape (Demtröder, 2014):

$$\Re(\nu, T) = \frac{2}{\Delta\nu_D(T)} \cdot \sqrt{\frac{ln\,2}{\pi}} \cdot exp\left[\frac{-4\,ln\,2(\nu-\nu_0-\Delta\nu)^2}{\Delta\nu_D^2(T)}\right], \quad (2)$$

$$\Delta\nu_D(T) = \sqrt{\frac{8kT\,ln\,2}{mc^2}} \cdot \nu_0\,, \quad (3)$$

where k is the Boltzmann constant, m is the mean molecular mass of air, and c is the speed of light in vacuum.

In actual observations, the transmittance T_{obs} of atmospheric backscatter through the iodine cell is calculated as the ratio of the background- and dark-count-corrected photon counts in the iodine-cell channel $N_{atm,I2}$, to those in the reference channel $N_{atm,ref}$:

$$T_{obs} = \frac{N_{atm,I2}}{N_{atm,ref}}\,, \quad (4)$$

The measured transmittance T_{obs} is substituted into the inverse of the theoretical frequency–transmittance response function F^{-1}, to retrieve the Doppler frequency shift $\Delta\nu$ and the horizontal LOS wind speed V_{HLOS}:

$$\Delta\nu = F^{-1}(T_{obs}, \nu_0, T)\,, \quad (5)$$

$$V_{HLOS} = \frac{\lambda\Delta\nu}{2\sin\gamma}\,, \quad (6)$$

where λ is the transmitted laser wavelength and γ is the off-zenith angle.

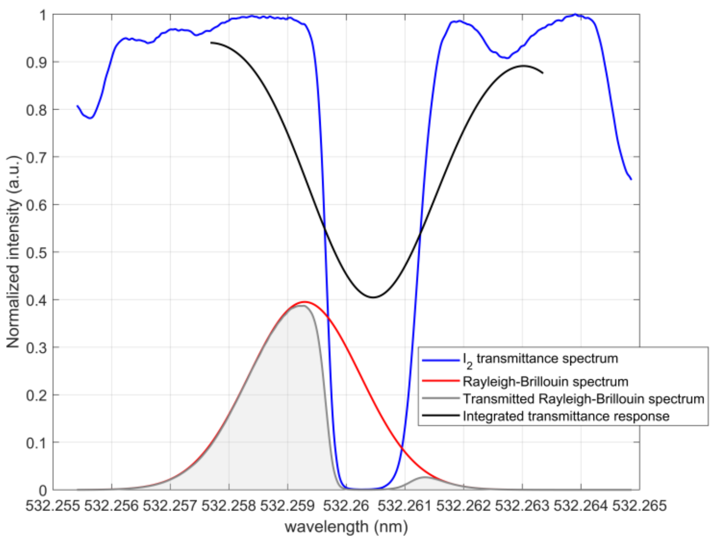

Figure 5: Principle of single-edge Doppler frequency discrimination using an iodine absorption cell. The blue curve shows the normalized iodine transmittance spectrum, the red curve shows the Cabannes line, the gray shaded area indicates the transmitted spectrum of the Cabannes line after passing through the iodine cell, and the black curve represents the normalized transmittance response for Cabannes lines with different center frequencies.

https://doi.org/10.5194/egusphere-2026-5021
Preprint. Discussion started: 25 August 2026

3.2 Zero-Doppler reference measurement and wind correction

The DFDR configuration in Fig.2 allows the seed reference light and atmospheric backscatter to share the same iodine-cell frequency discriminator and detection channels. Therefore, measuring the transmittance T_{seed} of the seed reference light through the iodine cell provides the relative spectral position of the seed laser with respect to the current frequency-discrimination response. Figure 5 shows an approximately linear region near the steep edge of the iodine absorption line, which is selected as the locking range for the seed laser frequency. By pre-calibrating the relationship between the seed-reference transmittance and laser frequency, the measured T_{seed} can be converted into an equivalent laser frequency $\nu_{laser,I2}$, which represents the spectral position of the laser frequency on the frequency–transmittance response curve of the discriminator:

$$\nu_{laser,I_2} = aT_{seed} + b \, , \tag{7}$$

where a and b are the slope and intercept of the linear fit, respectively.

During a complete RDLD observation and retrieval cycle, the VT channel first completes its measurement and retrieves the atmospheric temperature profile T. At this stage, the WT and NT measurements have not yet been completed, and the corresponding actual seed-reference transmittances are therefore not yet available. To construct the theoretical frequency–transmittance response function required for wind retrieval in advance, a reference seed transmittance $T_{seed,ref}$ close to the nominal operating point is predefined, and the corresponding reference frequency $\nu_{0,ref}$ is determined using Eq. (7). This frequency $\nu_{0,ref}$ serves as the predefined zero-Doppler reference for calculating the theoretical response function F. After the WT and NT measurements are completed, the Doppler frequency shift $\Delta\nu_{retr}$ relative to the predefined zero-Doppler baseline $\Delta\nu_{0,ref}$ is first retrieved from the pre-calculated response function F and the measured atmospheric-backscatter transmittance T_{obs}. Meanwhile, the synchronously measured seed-reference transmittance $T_{seed,real}$ is used to determine the actual equivalent laser frequency $\nu_{laser,real}$ relative to the discriminator response. The difference between $\nu_{laser,real}$ and the predefined zero-Doppler reference $\Delta\nu_{0,ref}$ν is defined as the zero-Doppler reference offset $\Delta\nu_0$:

$$\Delta\nu_0 = \nu_{laser,real} - \nu_{0,ref} \, , \tag{8}$$

Because the initially retrieved Doppler frequency shift $\Delta\nu_{retr}$ is referenced to the predefined zero-Doppler reference $\Delta\nu_{0,ref}$, it includes both the actual atmospheric Doppler shift and the offset introduced by the shift in the zero-Doppler reference. The corrected Doppler frequency shift $\Delta\nu_{corr}$ is therefore obtained by subtracting $\Delta\nu_0$:

$$\Delta\nu_{corr} = \Delta\nu_{retr} - \Delta\nu_0 \, , \tag{9}$$

https://doi.org/10.5194/egusphere-2026-5021
Preprint. Discussion started: 25 August 2026

4 Experiments and results

4.1 Validation of zero-Doppler reference measurement and tracking

The frequency–transmittance response of the iodine cell was calibrated experimentally. During the calibration, the seed laser (SL) operated in frequency-scanning mode, with the seed reference light scanned across the iodine 1109 absorption line. During the scan, the DFDR measured the transmittance of the seed reference light through the iodine cell, while a wavemeter (HighFinesse, WS7-60) simultaneously measured its wavelength. The frequency-tuning signal applied to the SL was a sawtooth waveform with a period of 200 s. The seed-reference wavelength was scanned over a range of approximately 10 pm centered at about 532.26 nm. The integration time for each sampling point was 100 ms, and the wavemeter exposure time was also 100 ms. Approximately 2000 sampling points were obtained during each scan cycle, with an average wavelength interval of about 5 fm between adjacent points, corresponding to a frequency interval of approximately 5 MHz. The specified relative frequency resolution of the WS7-60 wavemeter is 2 MHz, which is smaller than the frequency interval between adjacent sampling points. This configuration therefore provides sufficiently dense sampling of the iodine transmittance spectrum. Figure 6(a) shows the calibrated iodine frequency–transmittance response of the DFDR seed-reference channel, clearly revealing the iodine 1109 absorption line. Because the calibration is performed directly on the DFDR, system-specific factors such as optical efficiency, beam-splitting ratio, and photomultiplier-tube detection efficiency are inherently incorporated into the calibrated response. These parameters therefore do not require separate calibration. Figure 6(b) shows the linear fit over the selected operating range on the edge of the iodine-cell frequency–transmittance response curve, which is used to establish the conversion between seed-reference transmittance and wavelength. Within this range, transmittance and wavelength exhibit a strong linear relationship, with a coefficient of determination R^2 of 0.9979 and a wavelength root-mean-square error (RMSE) of 3.147×10^{-6} nm, corresponding to an equivalent frequency RMSE of approximately 3.33 MHz. The fitted slope p_1 is -7.459×10^{-4} nm a.u.$^{-1}$, representing the conversion coefficient from seed-reference transmittance to wavelength within the operating range. According to the wavelength–frequency conversion relation, the transmittance-to-frequency conversion coefficient is approximately 789 MHz a.u.$^{-1}$, meaning that a transmittance change of 0.001 corresponds to a frequency change of approximately 0.789 MHz. Therefore, if the DFDR achieves a measurement stability of 10^{-3} in seed-reference transmittance, it should theoretically be capable of resolving megahertz-scale variations in the laser frequency. As shown in Fig. 6(c), the fitting residuals are mainly distributed around zero, with no evident overall bias. The mean residual is approximately 4.87×10^{-14} nm, corresponding to an equivalent frequency offset of approximately 5.16×10^{-8} MHz. These results indicate that the linear fit accurately represents the relationship between transmittance and frequency within the selected operating range.

https://doi.org/10.5194/egusphere-2026-5021
Preprint. Discussion started: 25 August 2026

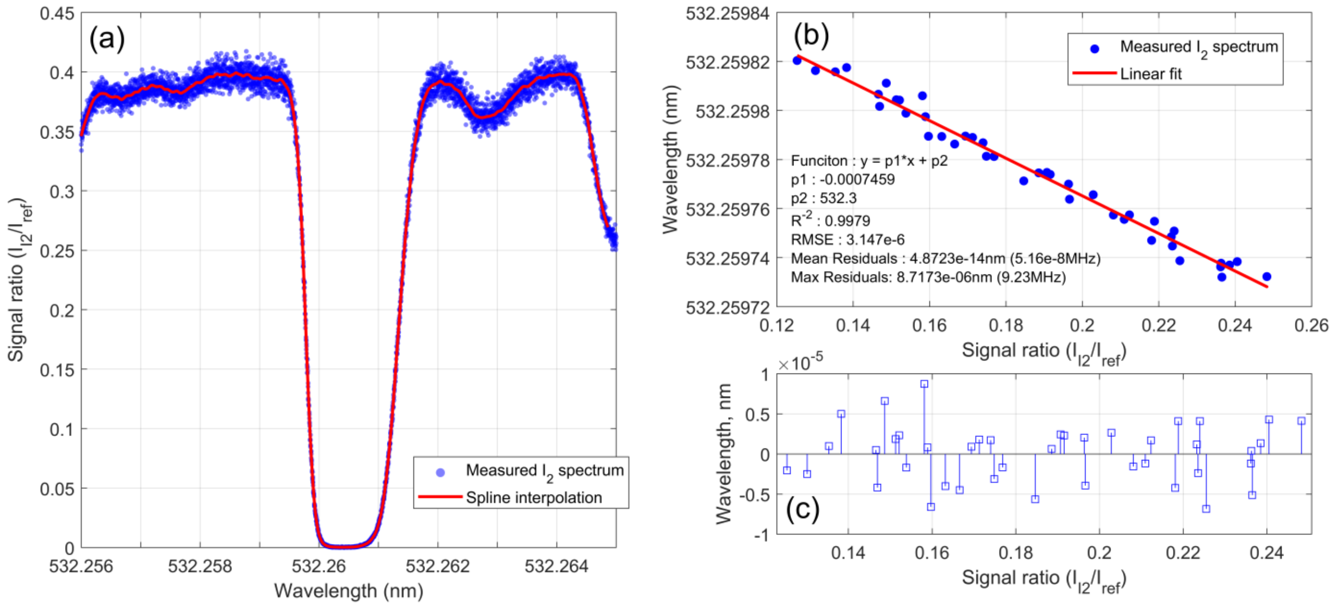

Figure 6: Calibration results of the iodine frequency–transmittance response for the DFDR seed-reference channel. (a) Equivalent iodine transmittance response measured in the seed-reference channel. The blue dots represent the raw experimental data, and the red curve represents the spline interpolation. (b) Linear fit between transmittance and wavelength over the selected linear region of the iodine frequency–transmittance response curve. (c) Residuals of the linear fit in (b)

Figure 7(a) shows the results of a dynamic frequency-tracking experiment in which the seed-laser wavelength was varied by adjusting the DFB-laser temperature. The DFDR-retrieved wavelengths were compared with synchronous wavemeter measurements. The DFDR continuously tracked the seed-reference wavelength during the initial slow drift, the rapid variation around 10 min, and the subsequent damped oscillation after relocking. Overall, the DFDR retrievals and wavemeter measurements showed consistent temporal variations. Figure 7(b) shows the difference between the DFDR-retrieved and wavemeter-measured wavelengths. Throughout the experiment, the tracking difference fluctuated around zero without a persistent one-sided offset. The fluctuations increased during the rapid wavelength change and relocking transition, but remained generally stable. The standard deviation of the tracking difference was 1.186 fm, corresponding to a frequency standard deviation of 1.25 MHz. Based on the transmittance-to-frequency conversion coefficient derived from Fig. 6(b), this frequency standard deviation corresponds to an equivalent transmittance variation of approximately 1.6×10^{-3}. This result indicates that, with an integration time of 100 ms, the DFDR can resolve seed-reference transmittance variations on the order of 10^{-3}. Figure 7(c) further shows the scatter relationship between the two measurements. The data points are distributed close to the 1:1 line, with a fitted slope of 0.9745 and a coefficient of determination R^2 of 0.935, indicating good agreement between the DFDR-retrieved and wavemeter-measured wavelengths. These results demonstrate that the DFDR can continuously track dynamic variations in the seed-reference wavelength.

https://doi.org/10.5194/egusphere-2026-5021
Preprint. Discussion started: 25 August 2026

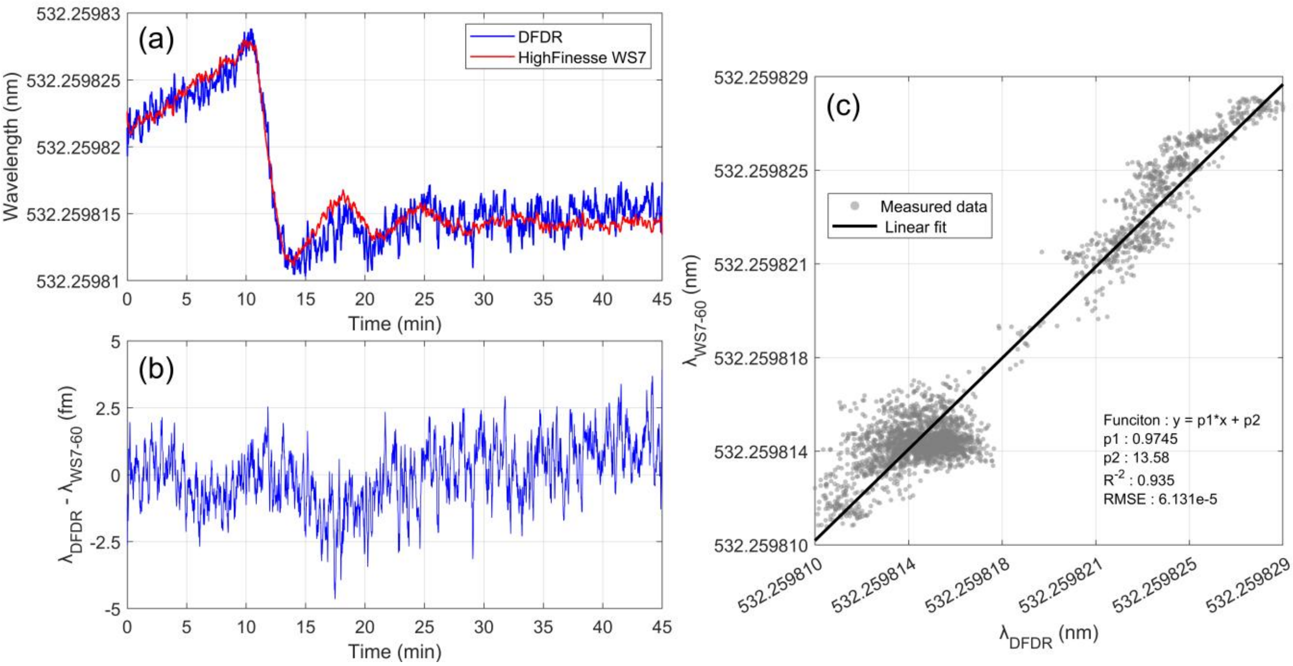

Figure 7: Validation results of the DFDR wavelength measurement. (a) Time-series comparison between the DFDR-retrieved and wavemeter-measured wavelengths. (b) Difference between the two wavelength measurements. (c) Linear relationship between the DFDR-retrieved and wavemeter-measured wavelengths

4.1.2 Long-term zero-Doppler reference tracking

Figure 8(a) presents an 8 h continuous measurement under seed laser frequency locking to evaluate the long-term zero-Doppler reference tracking performance of the DFDR. The wavemeter measurements remained generally stable, whereas the DFDR retrievals exhibited additional slow variations on hourly timescales, indicating that the spectral position of the seed laser relative to the DFDR frequency-discrimination response may still drift over extended periods.

The frequency difference between the DFDR and wavemeter measurements is presented in Fig. 8(b). The raw frequency difference fluctuated around zero throughout the experiment, with no abrupt jumps observed. To approximate the temporal resolution used in routine observations, a 300 s moving average was applied to the frequency difference. The smoothed frequency difference exhibited slow variations on hourly timescales, with an 8 h mean of −0.10 MHz, indicating no evident long-term fixed bias between the two measurements. Its standard deviation was 1.901 MHz, and the peak-to-peak variation reached 7.307 MHz, indicating megahertz-scale changes in the spectral position of the laser relative to the DFDR frequency-discrimination response over several hours. Since the seed-laser frequency measured by the wavemeter varied only slightly during the same period, these low-frequency differences mainly reflect slow changes in the DFDR frequency-discrimination response relative to the laser frequency. Possible sources include small drifts in the iodine-cell temperature, changes in the mechanical state of the optical path, and long-term variations in the relative responses of the two detection channels. As an estimate of the resulting impact on wind measurements, the standard deviation of 1.901 MHz and the peak-to-peak variation

https://doi.org/10.5194/egusphere-2026-5021
Preprint. Discussion started: 25 August 2026

of 7.307 MHz correspond to equivalent LOS wind speeds of approximately 0.51 and 1.94 m s^{-1}, respectively. These results indicate that long-term variations in the zero-Doppler reference can have a non-negligible impact on high-precision wind measurements. The wavemeter exhibits consistently lower Allan deviations than the DFDR, indicating higher random noise in the DFDR measurements at short timescales, which is associated with frequency retrieval based on the ratio of photon counts from the two detection channels.

Figure 8(c) shows the Allan deviations of the DFDR and wavemeter measurements, which are used to evaluate frequency-measurement stability at different averaging times. At shorter averaging times, the Allan deviations of both measurements decrease with increasing averaging time, indicating that longer integration effectively suppresses random measurement noise. The wavemeter exhibits consistently lower Allan deviations than the DFDR, indicating higher random noise in the DFDR measurements at short timescales, which is associated with frequency retrieval based on the ratio of photon counts from the two detection channels. For the DFDR, the Allan deviation remains relatively low over averaging times of 100–1000 s, with a mean value of approximately 0.29 MHz. This indicates that minute-scale integration substantially improves the short-term stability of zero-Doppler reference measurements. At longer averaging times, the DFDR Allan deviation gradually levels off and then increases, consistent with the hour-scale low-frequency variations observed in Fig. 8(b), indicating that the measurement stability is increasingly affected by slow system variations.

These results demonstrate that the DFDR can stably track variations in the spectral position of the seed laser relative to the frequency-discrimination response during several hours of continuous observation. More importantly, even with the seed-laser frequency locked, the DFDR detected hour-scale relative spectral variations of several megahertz, indicating that the zero-Doppler reference may not remain strictly constant during long-term observations. Online measurement and updating of the zero-Doppler reference can therefore help reduce biases in wind retrieval caused by slow system variations. In practical observations, setting the signal integration time of each channel within the range of 100–1000 s provides a reasonable balance among random-noise suppression, the influence of slow system variations, and temporal resolution.

https://doi.org/10.5194/egusphere-2026-5021
Preprint. Discussion started: 25 August 2026

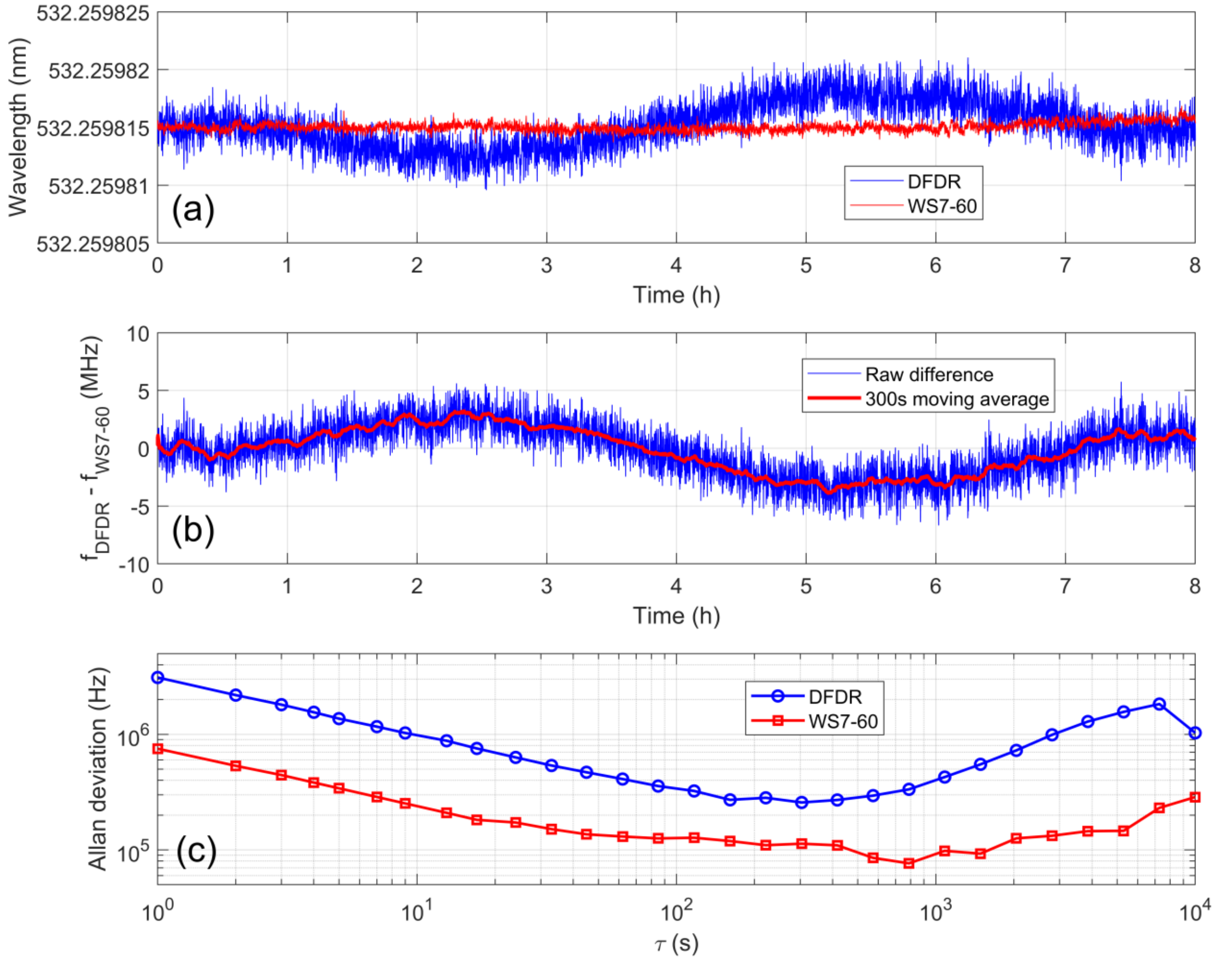

305 **Figure 8: Long-term tracking stability of the DFDR zero-Doppler reference. (a) Time series of the DFDR and wavemeter measurements. (b) Frequency difference between the two measurements. The blue line represents the raw frequency difference, and the red line represents the 300 s moving average. (c) Allan deviations of the two measurements.**

4.1.3 Frequency consistency between the seed laser and pulsed laser

Figure 9(a) compares the wavelengths of the 532nm seed-reference light and emitted pulsed laser measured synchronously with two wavemeters (HighFinesse, WS7-60). During the first 80 min, the laser remained frequency locked, followed by a small-range frequency tuning. The seed-reference light and pulsed laser wavelengths remained consistent throughout, with no evident tracking lag or abrupt frequency jumps. Figure 9(b) shows the frequency difference between the seed-reference light and the pulsed laser, which remained centered near 0 MHz with most values within ±4 MHz. The distribution in Fig. 9(c) is approximately Gaussian, with a mean near 0 MHz and a standard deviation of 1.14 MHz, indicating good frequency

https://doi.org/10.5194/egusphere-2026-5021
Preprint. Discussion started: 25 August 2026

consistency without an evident systematic offset. These results support the use of the seed-reference light to represent the emitted pulsed laser frequency.

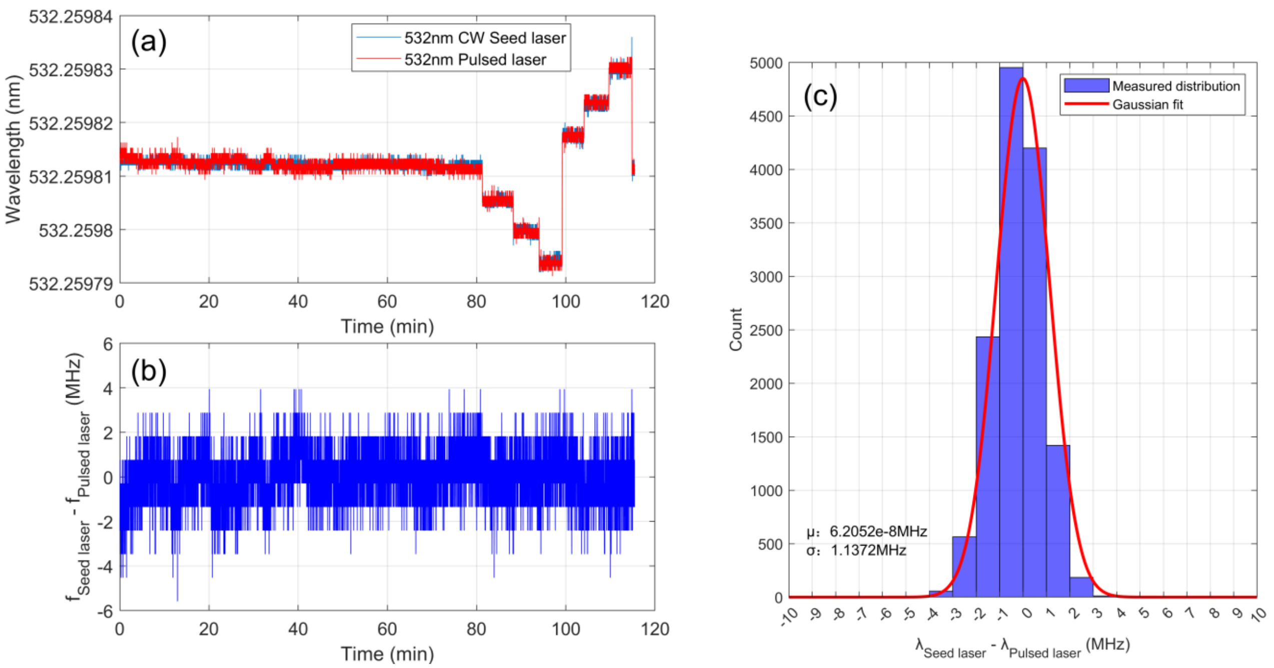

Figure 9: Frequency consistency between the seed reference light and pulsed laser. (a) Time series of the wavelengths of the 532 nm continuous seed reference light (blue) and pulsed laser (red). (b) Wavelength difference between the seed reference light and pulsed laser. (c) Histogram of the wavelength difference and corresponding Gaussian fit.

4.2 Validation of wind correction

In the stratosphere and mesosphere, vertical winds are generally much weaker than horizontal winds and are expected to average close to zero over appropriate temporal and vertical scales. Vertical-channel measurements can therefore provide a useful reference for evaluating zero-Doppler reference offsets, as adopted in previous RDLD studies for calibration and validation (Souprayen et al., 1999; Fiedler et al., 1999). This study evaluates the proposed method by comparing the overall vertical-wind offset before and after zero-Doppler reference correction.

Figure 10 presents the nighttime vertical-wind observations and the corresponding intermediate variables used for zero-Doppler reference correction. Figure 10(a) shows the vertical winds retrieved without zero-Doppler reference correction. The persistent positive offset over most times and altitudes between 30 and 50 km suggests a common zero-Doppler reference error, rather than purely atmospheric vertical motions. Fig. 10(d) gives the time series of the synchronously measured seed-reference transmittance and the corresponding wind correction. The measured seed-reference transmittance remained higher than the predefined reference value throughout the observation and varied with time. The measured seed-laser frequency was used to determine the offset from the predefined zero-Doppler reference and the corresponding wind correction. During this observation, the wind correction ranged from approximately −1.0 to −2.5 m s^{-1}. This indicates that retrieval using the

https://doi.org/10.5194/egusphere-2026-5021
Preprint. Discussion started: 25 August 2026

predefined zero-Doppler reference introduces a positive wind bias, consistent with the overall positive offset observed in Fig. 10(a).Figure 10(b) indicates that the zero-Doppler reference correction substantially reduces the persistent positive offset and yields a more balanced distribution of positive and negative vertical winds. Figure 10(c) quantifies this improvement, with the mean vertical wind over 30–50 km shifting from approximately 1.2 to −0.34 m s^{-1} after correction, demonstrating that online zero-Doppler reference determination substantially reduces the overall vertical-wind bias. The corrected vertical winds do not strictly converge to zero, and the remaining fluctuations may reflect both real atmospheric vertical motions, such as gravity-wave-induced perturbations, and measurement uncertainties.

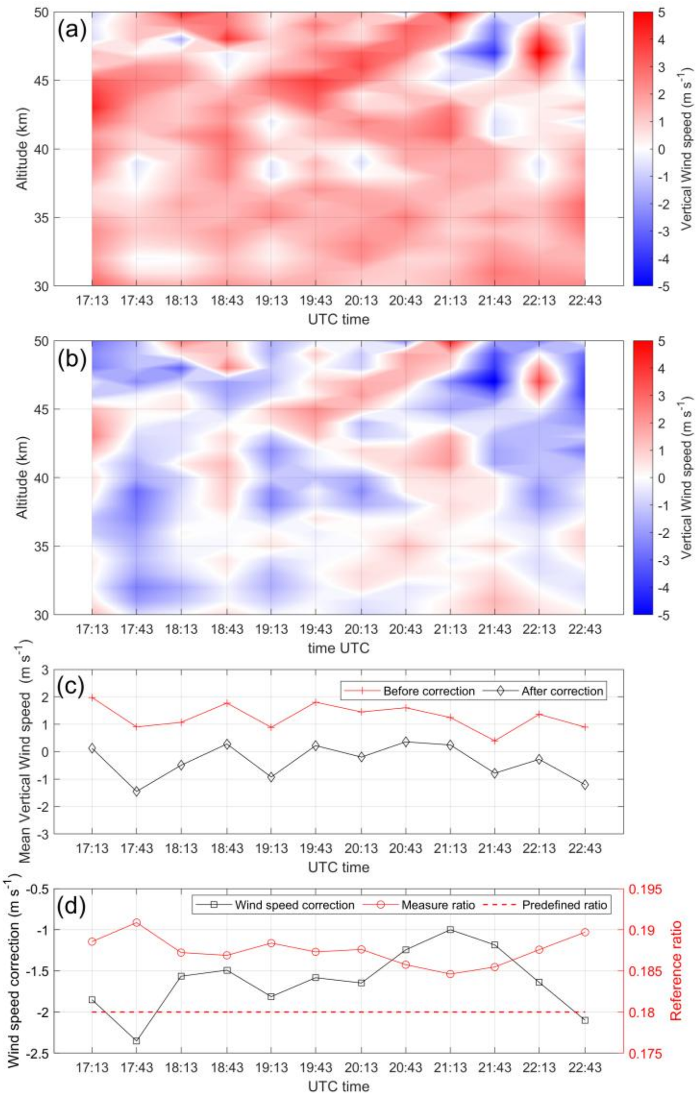

Figure 10: Vertical-wind observations and zero-Doppler reference correction on 11 February 2026. (a) Vertical winds before correction. (b) Vertical winds after correction. (c) Mean vertical winds over 30–50 km before (red crosses) and after (black diamonds) correction. (d) Time series of the measured seed-reference transmittance (red circles, right axis) and wind correction (black squares, left axis); the red dashed line indicates the predefined seed-reference transmittance.

https://doi.org/10.5194/egusphere-2026-5021
Preprint. Discussion started: 25 August 2026

4.3 Validation of Doppler-shift measurement

To further validate the DFDR response to known frequency offsets, we introduced controlled static shifts in the transmitted laser frequency by changing the target transmittance of the iodine cell used for seed-laser frequency locking. The retrieved vertical winds were compared with theoretical equivalent winds derived from wavemeter-measured frequency offsets. Because the equivalent winds corresponding to the imposed frequency offsets were much larger than the typical mean vertical wind, the observed profile shifts were dominated by the introduced laser-frequency offsets.

Three locking transmittances of 30%, 45%, and 75% were used in the experiment. Before the experiment, the laser frequencies under the three locking conditions were measured with a wavemeter. Taking the 30% locking condition as the reference operating point, the relative frequency offsets at 45% and 75% were calculated and converted into theoretical equivalent winds using Eq. (6), as summarized in Table 1. Figure 11 compares the vertical-wind profiles under the three locking conditions. While their local vertical structures remain similar, the profiles shift systematically with locking frequency. The mean vertical winds are −0.06, 12.06, and 37.91 m s^{-1} at 30%, 45%, and 75% transmittance, respectively. The latter tow agree well with the theoretical equivalent winds of 11.02 and 37.49 m s^{-1}, respectively.

Table 1. relative frequency offsets and theoretical and measured equivalent wind speeds under different locking transmittances

Locking transmittance	Relative frequency offset	Theoretical equivalent wind speed	Measured mean wind speed	Difference
30% (reference)	0 MHz	0 m s^{-1}	-0.06 m s^{-1}	-0.06 m s^{-1}
45%	41.48 MHz	11.02 m s^{-1}	12.06 m s^{-1}	1.04 m s^{-1}
75%	140.96 MHz	37.49 m s^{-1}	37.91 m s^{-1}	0.42 m s^{-1}

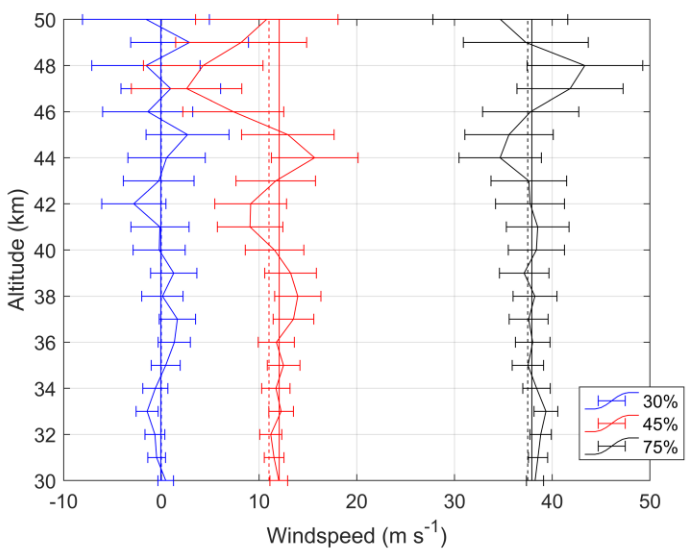

Figure 11: Vertical-wind retrievals under controlled laser-frequency offsets at 15:00 UTC on 11 February 2026. The blue, red, and black profiles correspond to locking transmittances of 30%, 45%, and 75%, respectively; error bars indicate retrieval uncertainties.

https://doi.org/10.5194/egusphere-2026-5021
Preprint. Discussion started: 25 August 2026

Solid lines indicate the mean measured winds over 30–50 km, and dashed lines indicate the theoretical equivalent winds derived from wavemeter-measured relative frequency offsets.

Figure 12 validates the theoretical frequency–transmittance response function using a temperature–transmittance–wind map, with the background colors representing calculated LOS wind speeds and the black curves representing equivalent-wind contours. The contours at 0, 11.02, and 37.49 m s^{-1} correspond to the theoretical equivalent winds derived from the wavemeter-measured relative laser-frequency offsets under the 30%, 45%, and 75% locking conditions, respectively. The measured transmittances and corresponding temperatures under the three locking conditions cluster near their respective theoretical equivalent-wind contours. The measured temperature dependence agrees well with the theoretical contours, indicating that the response function adequately captures the relationship among temperature, iodine-cell transmittance, and LOS wind speed. Together with Fig. 11, these results show that the DFDR correctly responds to known laser-frequency offsets and that the theoretical response reproduces the observed transmittance variations, further validating the RDLD wind retrieval method.

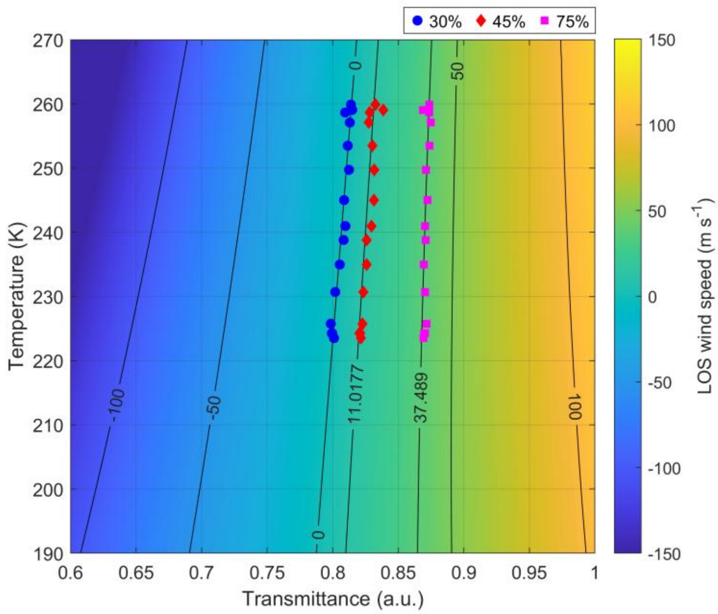

Figure 12: Comparison between the theoretical temperature–transmittance–LOS wind mapping and measurements. The background colors represent theoretical LOS wind speeds, and the black curves indicate equivalent-wind contours. Blue circles, red diamonds, and purple squares represent the measured atmospheric-backscatter transmittances and corresponding temperatures under the 30%, 45%, and 75% locking conditions, respectively.

4.4 Comparison of zonal and meridional winds with ERA5 reanalysis

To evaluate the RDLD performance in horizontal-wind observations, zonal and meridional winds measured during three consecutive nights from 11 to 13 February 2026 were compared with concurrent ERA5 reanalysis. The RDLD wind measurements have a temporal resolution of 30 min and a vertical resolution of 1 km. ERA5 data have a temporal resolution of 1 h and use the T137 model-level vertical grid (Hersbach et al., 2020). For spatial matching, the ERA5 profile at the grid

https://doi.org/10.5194/egusphere-2026-5021
Preprint. Discussion started: 25 August 2026

point nearest to the RDLD site was selected, and the ERA5 wind profiles were vertically interpolated to the RDLD observation altitudes. RDLD measurements with wind-retrieval uncertainties above 30 m s^{-1}were excluded from the comparison.

Figures 13 and 14 show that the major zonal- and meridional-wind structures observed by the RDLD exhibit temporal evolution similar to that in ERA5. For example, Figs. 13(c) and 13(f) show that after 15:00 UTC on 13 February, the zonal wind between 35 and 50 km gradually weakened and reversed direction, followed by a further strengthening of the easterly wind. For the meridional wind, Figs. 14(b) and 14(e) show alternating positive and negative wind layers below 50 km on 12 February. A positive-wind layer near 40–45 km persisted for a relatively long period and exhibited a downward displacement with time. Compared with ERA5, the RDLD observations resolve more local and short-timescale wind variability owing to their higher temporal and vertical resolutions.

Figures 15 and 16 further compare the corresponding daily mean wind profiles and the ranges of wind variation within each day. Between 30 and 55 km, the RDLD and ERA5 show generally consistent daily mean winds and major vertical structures. Above 55 km, the differences gradually increase, accompanied by a clear increase in the daily variation range of the RDLD measurements. These discrepancies may reflect differences in spatial representativeness and resolution between the two datasets, as well as reduced RDLD signal-to-noise ratio and increased wind-retrieval uncertainty at higher altitudes.

Overall, the three-night comparison shows that the RDLD and ERA5 generally agree in the vertical structure and magnitude of the horizontal winds between 30 and 60 km. Because the RDLD provides local remote-sensing observations whereas ERA5 represents a reanalysis background field over a broader spatial scale, complete agreement cannot be expected at all times and altitudes (Dou et al., 2014; Baumgarten et al., 2015; Gisinger et al., 2022). Nevertheless, the comparison indicates that, after online zero-Doppler reference tracking and wind correction, the RDLD can reliably retrieve stratospheric and mesospheric horizontal winds with reasonable vertical structures and temporal evolution.

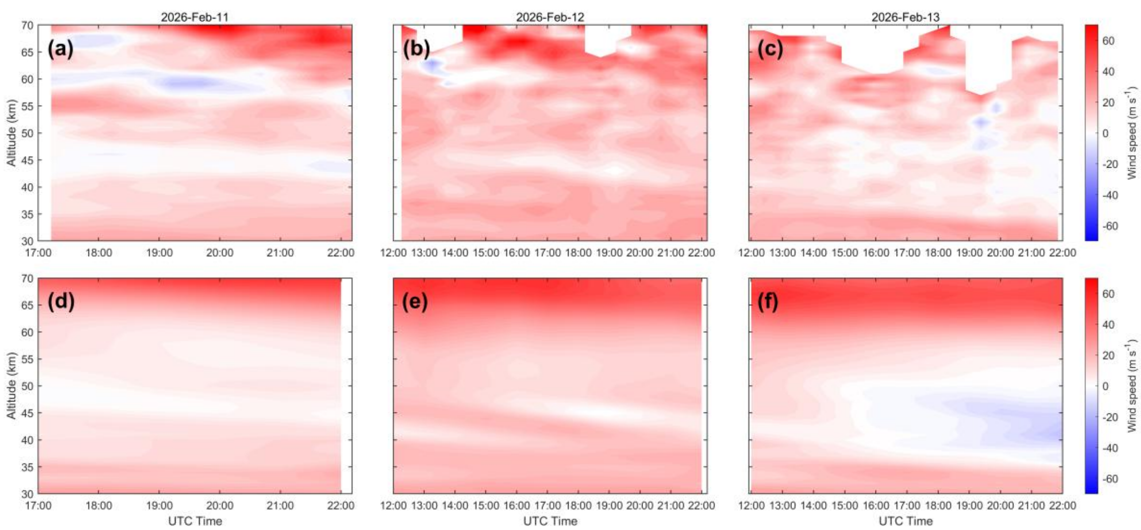

Figure 13: Comparison of zonal winds during three consecutive nights from 11 to 13 February 2026. (a–c) RDLD-retrieved zonal winds. (d–f) ERA5 reanalysis winds for the corresponding observation periods.

https://doi.org/10.5194/egusphere-2026-5021
Preprint. Discussion started: 25 August 2026

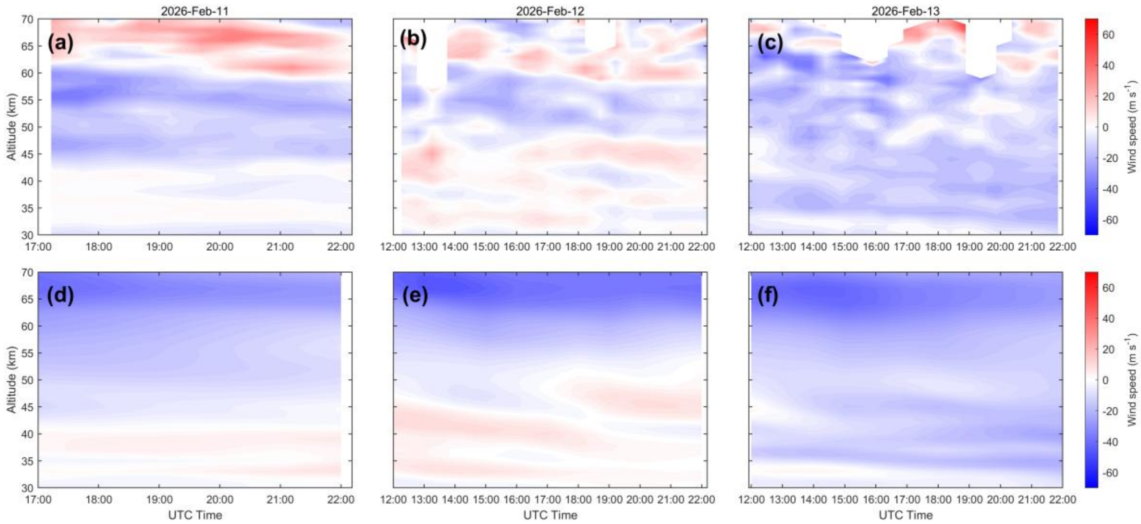

410 **Figure 14: Comparison of meridional winds. The panel arrangement is the same as in Fig. 13.**

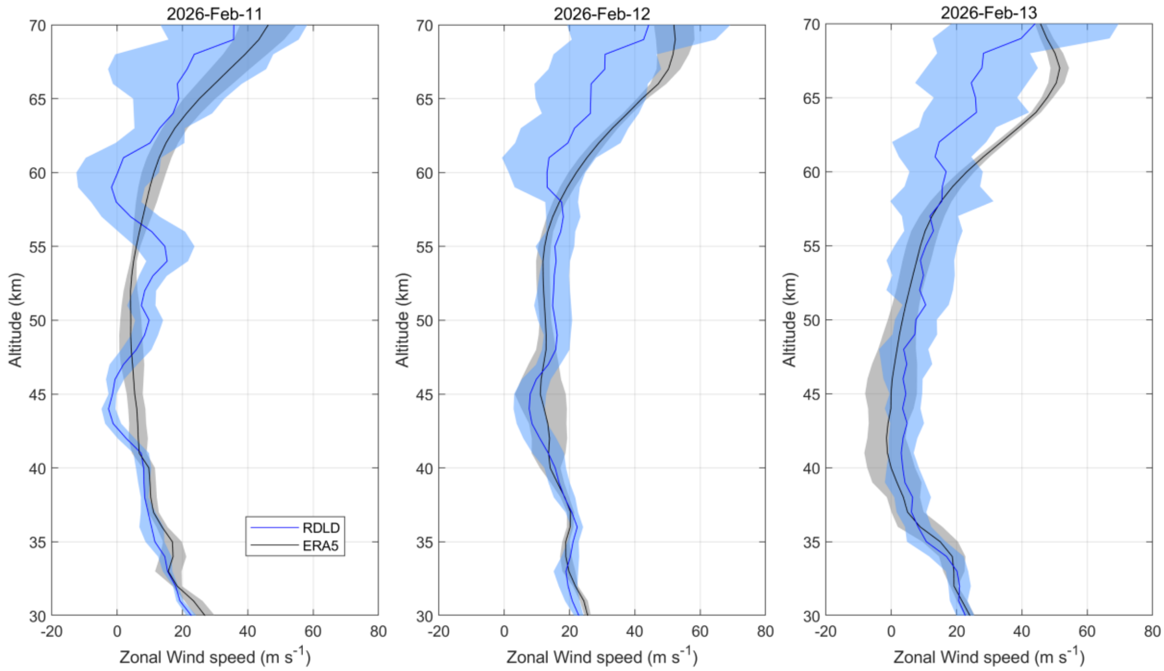

Figure 15: Comparison of nighttime-mean zonal-wind profiles from the RDLD and ERA5 over three nights. Blue and black solid lines represent the RDLD and ERA5 nighttime means, respectively, with the corresponding shaded areas indicating ±1 standard deviation of the nighttime wind variability.

415

https://doi.org/10.5194/egusphere-2026-5021
Preprint. Discussion started: 25 August 2026

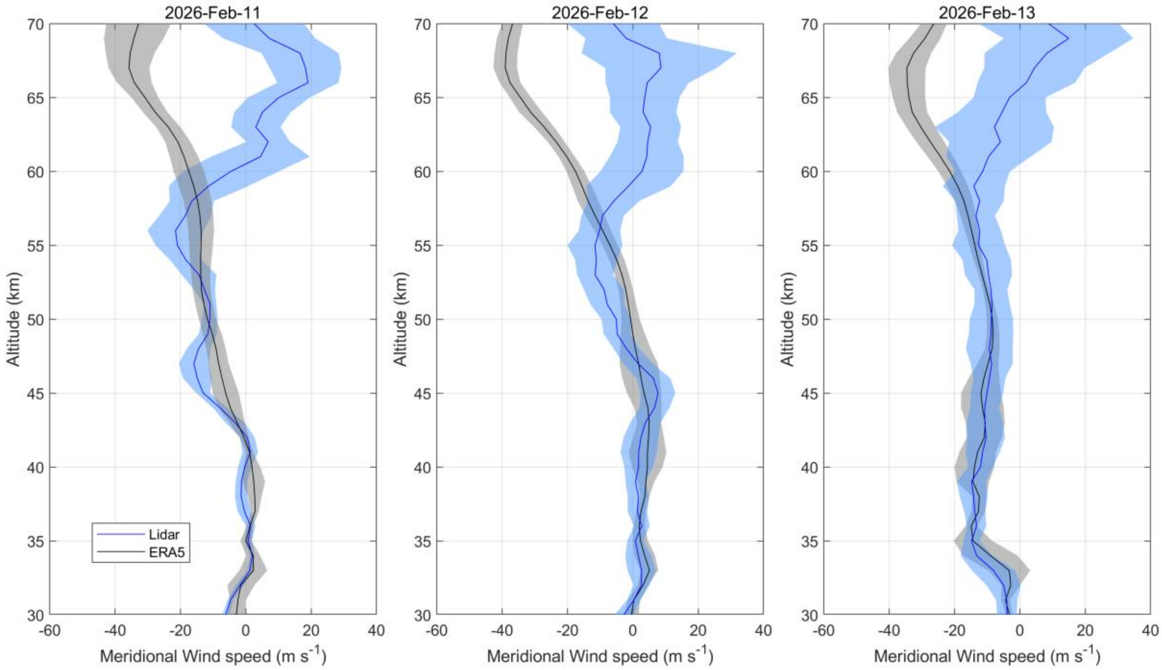

Figure 16: Nighttime-mean meridional-wind profiles. Colors and shading are as in Fig. 15.

5 Conclusion

To address zero-Doppler reference shifts caused by slow drifts in laser frequency and discriminator response, this study develops and validates an online tracking and wind correction method for an iodine-cell Rayleigh Doppler lidar. Using time-division multiplexing, the seed reference light and atmospheric backscatter share the same iodine-cell frequency discriminator. The seed-reference transmittance is used to determine the transmitted laser position on the current frequency–transmittance response curve, enabling online tracking of the relative spectral position and correction of Doppler wind retrievals. Thus, the zero-Doppler reference is treated as a continuously monitored and updated system state rather than a fixed calibration parameter.

The frequency-tracking capability and long-term zero-Doppler reference tracking performance were validated experimentally. The DFDR tracked dynamic seed-laser frequency variations with a standard deviation of 1.255 MHz relative to the wavemeter measurements. An 8 h continuous measurement revealed hour-scale relative spectral variations of several megahertz between the transmitted laser and discriminator response, indicating that the zero-Doppler reference may drift during long-term operation. The Allan deviation of the DFDR frequency measurements decreased to approximately 0.29 MHz for integration times of 100–1000 s. The seed reference light and pulsed laser showed a frequency-difference standard deviation of 1.137 MHz, supporting the use of the seed reference light to track pulsed-laser frequency variations.

https://doi.org/10.5194/egusphere-2026-5021
Preprint. Discussion started: 25 August 2026

The method also performed well in atmospheric observations. Before correction, the retrieved vertical winds showed a persistent positive bias, with corresponding wind corrections of approximately −1.0 to −2.5 m s^{-1}. After correction, the mean vertical wind shifted from 1.2 to −0.34 m s^{-1}, substantially reducing the systematic bias. In the controlled frequency-offset experiment, the RDLD-retrieved equivalent winds agreed well with the theoretical values derived from independently measured wavemeter frequency offsets, further validating the wind retrieval method. The measured zonal and meridional winds also showed good agreement with ERA5 reanalysis in their major vertical structures and temporal evolution.

In summary, this study establishes and validates a complete processing scheme from receiver-side seed-reference measurement and online zero-Doppler reference updating to wind correction. The method enables online tracking and correction of the zero-Doppler reference for iodine-cell RDLD without continuous reliance on an external wavemeter. The system is currently used for routine observations, and longer-term measurements will be used to further evaluate the method and provide reliable wind observations for studies of stratospheric and mesospheric dynamics.

Data availability

The lidar data underlying the results presented in this study are available from the corresponding author upon reasonable request. The ERA5 reanalysis data used in this study are publicly available from the Copernicus Climate Change Service (C3S) Climate Data Store (CDS) through the "Complete ERA5 global atmospheric reanalysis" dataset (https://doi.org/10.24381/cds.143582cf).

Author contributions

TZ conceived the study, carried out the investigation, performed the formal analysis and visualization, and prepared the manuscript. SS contributed to the formal analysis and validation, as well as manuscript reviewed and edited. BL acquired the funding and supervised the research. YB was responsible for project administration with contributions to formal analysis, visualization, and manuscript review and editing. HC, WY, and WC provided experimental resources and contributed to manuscript reviewed and edited. All authors participated in the discussion of the results and approved the final version of the manuscript.

Acknowledgements

We gratefully acknowledge the National Satellite Meteorological Center (National Center for Space Weather) of the China Meteorological Administration and the Jiuquan National Reference Climatological Station for their support during the experiments. We also thank Nanjing Movelaser Company for providing technical support. We acknowledge the Copernicus

Climate Change Service (C3S) at the European Centre for Medium-Range Weather Forecasts (ECMWF) for providing the ERA5 reanalysis data used in this study.

Financial support

This research was supported by the Jing-Jin-Ji Regional Integrated Environmental Improvement–National Science and Technology Major Project of the Ministry of Ecology and Environment of China (grant no. 2025ZD1200900) and the Open Research Fund of the Key Laboratory of Intelligent Support Technology for Complex Environments, Ministry of Education, Nanjing University of Information Science and Technology.

References

Baumgarten, G.: Doppler Rayleigh/Mie/Raman lidar for wind and temperature measurements in the middle atmosphere up to 80 km, Atmos. Meas. Tech., 3, 1509–1518, https://doi.org/10.5194/amt-3-1509-2010, 2010.

Baumgarten, G., Fiedler, J., Hildebrand, J., and Lübken, F.-J.: Inertia gravity wave in the stratosphere and mesosphere observed by Doppler wind and temperature lidar, Geophys. Res. Lett., 42, 10929–10936, https://doi.org/10.1002/2015GL066991, 2015.

Demtröder, W.: Laser Spectroscopy 1: Basic Principles, 5th edn., Vol. 1, Springer, Berlin, Heidelberg, Germany, https://doi.org/10.1007/978-3-642-53859-9, 2014.

Di Donfrancesco, G., Adriani, A., Gobbi, G. P., and Congeduti, F.: Lidar observations of stratospheric temperature above McMurdo Station, Antarctica, J. Atmos. Terr. Phys., 58, 1391–1399, https://doi.org/10.1016/0021-9169(95)00164-6, 1996.

Dou, X., Han, Y., Sun, D., Xia, H., Shu, Z., Zhao, R., Shangguan, M., and Guo, J.: Mobile Rayleigh Doppler lidar for wind and temperature measurements in the stratosphere and lower mesosphere, Opt. Express, 22, A1203–A1221, https://doi.org/10.1364/OE.22.0A1203, 2014.

Ehard, B., Kaifler, B., Kaifler, N., and Rapp, M.: Evaluation of methods for gravity wave extraction from middle-atmospheric lidar temperature measurements, Atmos. Meas. Tech., 8, 4645–4655, https://doi.org/10.5194/amt-8-4645-2015, 2015.

Fiedler, J. and von Cossart, G.: Automated Lidar Transmitter for Multiparameter Investigations Within the Arctic Atmosphere, IEEE T. Geosci. Remote, 37, 748–755, 1999.

Fiedler, J. and Baumgarten, G.: The ALOMAR Rayleigh/Mie/Raman lidar: status after 30 years of operation, Atmos. Meas. Tech., 17, 5841–5859, https://doi.org/10.5194/amt-17-5841-2024, 2024.

Fiedler, J., Baumgarten, G., Gerding, M., Köpnick, T., Ostermann, R., and Kaifler, B.: Frequency control and monitoring of the ALOMAR RMR lidar's pulsed high-power Nd lasers, Geosci. Instrum. Method. Data Syst., 15, 17–26, https://doi.org/10.5194/gi-15-17-2026, 2026.

https://doi.org/10.5194/egusphere-2026-5021
Preprint. Discussion started: 25 August 2026

Gisinger, S., Polichtchouk, I., Dörnbrack, A., Reichert, R., Kaifler, B., Kaifler, N., Rapp, M., and Sandu, I.: Gravity-wave-driven seasonal variability of temperature differences between ECMWF IFS and Rayleigh lidar measurements in the lee of the Southern Andes, J. Geophys. Res.-Atmos., 127, e2021JD036270, https://doi.org/10.1029/2021JD036270, 2022.

Hauchecorne, A. and Chanin, M.-L.: Density and temperature profiles obtained by lidar between 35 and 70 km, Geophys. Res. Lett., 7, 565–568, https://doi.org/10.1029/GL007i008p00565, 1980.

Hersbach, H., Bell, B., Berrisford, P., Hirahara, S., Horányi, A., Muñoz-Sabater, J., Nicolas, J., Peubey, C., Radu, R., Schepers, D., Simmons, A., Soci, C., Abdalla, S., Abellan, X., Balsamo, G., Bechtold, P., Biavati, G., Bidlot, J., Bonavita, M., De Chiara, G., Dahlgren, P., Dee, D., Diamantakis, M., Dragani, R., Flemming, J., Forbes, R., Fuentes, M., Geer, A., Haimberger, L., Healy, S., Hogan, R. J., Hólm, E., Janisková, M., Keeley, S., Laloyaux, P., Lopez, P., Lupu, C., Radnoti, G., de Rosnay, P., Rozum, I., Vamborg, F., Villaume, S., and Thépaut, J.-N.: The ERA5 global reanalysis, Q. J. Roy. Meteor. Soc., 146, 1999–2049, https://doi.org/10.1002/qj.3803, 2020.

Hildebrand, J.: Wind and temperature measurements by Doppler Lidar in the Arctic middle atmosphere, PhD thesis, Universität Rostock, https://doi.org/10.18453/rosdok_id00001427, 2014.

Holton, J. R. and Hakim, G. J.: An Introduction to Dynamic Meteorology, 5th edn., Academic Press, Waltham, MA, USA, ISBN 978-0-12-384866-6, 2013.

Keckhut, P., Wild, J. D., Gelman, M., Miller, A. J., and Hauchecorne, A.: Investigations on long-term temperature changes in the upper stratosphere using lidar data and NCEP analyses, J. Geophys. Res.-Atmos., 106, 7937–7944, https://doi.org/10.1029/2000JD900845, 2001.

Khaykin, S. M., Hauchecorne, A., Mzé, N., and Keckhut, P.: Seasonal variation of gravity wave activity at midlatitudes from 7 years of COSMIC GPS and Rayleigh lidar temperature observations, Geophys. Res. Lett., 42, 1251–1258, https://doi.org/10.1002/2014GL062891, 2015.

Li, S., Ma, X., Li, H., Li, F., Zhu, X., and Chen, W.: Laser-diode-pumped zigzag slab Nd master oscillator power amplifier, Chin. Opt. Lett., 11, 071402, https://doi.org/10.3788/COL201311.071402, 2013.

Li, T., Fang, X., Liu, W., Gu, S.-Y., and Dou, X.: Narrowband sodium lidar for the measurements of mesopause region temperature and wind, Appl. Optics, 51, 5401–5411, https://doi.org/10.1364/AO.51.005401, 2012.

Liu, X., Xu, J., Yue, J., and Kogure, M.: Persistent layers of enhanced gravity wave dissipation in the upper mesosphere revealed from SABER observations, Geophys. Res. Lett., 49, e2021GL097038, https://doi.org/10.1029/2021GL097038, 2022.

Liu, Z. S., Wu, D., Liu, J. T., Zhang, K. L., Chen, W. B., Song, X. Q., Hair, J. W., and She, C. Y.: Low-altitude atmospheric wind measurement from the combined Mie and Rayleigh backscattering by Doppler lidar with an iodine filter, Appl. Optics, 41, 7079–7086, https://doi.org/10.1364/AO.41.007079, 2002.

Liu, Z., Wu, S., and Liu, B.: Seed injection and frequency-locked Nd laser for direct detection wind lidar, Opt. Laser Technol., 39, 541–545, https://doi.org/10.1016/j.optlastec.2005.10.010, 2007.

https://doi.org/10.5194/egusphere-2026-5021
Preprint. Discussion started: 25 August 2026

Mossad, M., Strelnikova, I., Wing, R., Baumgarten, G., and Gerding, M.: Spectral variability of gravity-wave kinetic and potential energy at 69° N: a seven-year lidar study, Atmos. Chem. Phys., 25, 14839–14864, https://doi.org/10.5194/acp-25-14839-2025, 2025.

Qiao, L., Chen, G., Zhang, S., Yao, Q., Gong, W., Su, M., Chen, F., Liu, E., Zhang, W., Zeng, H., Cai, X., Song, H., Zhang, H., and Zhang, L.: Wuhan MST radar: technical features and validation of wind observations, Atmos. Meas. Tech., 13, 5697–5713, https://doi.org/10.5194/amt-13-5697-2020, 2020.

Souprayen, C., Garnier, A., and Hertzog, A.: Rayleigh–Mie Doppler wind lidar for atmospheric measurements. II. Mie scattering effect, theory, and calibration, Appl. Optics, 38, 2422–2431, https://doi.org/10.1364/AO.38.002422, 1999.

Strelnikova, I., Almowafy, M., Baumgarten, G., Baumgarten, K., Ern, M., Gerding, M., and Lübken, F.-J.: Seasonal cycle of gravity wave potential energy densities from lidar and satellite observations at 54° and 69° N, J. Atmos. Sci., 78, 1359–1386, https://doi.org/10.1175/JAS-D-20-0247.1, 2021.

Tsutsumi, M. and Aso, T.: MF radar observations of meteors and meteor-derived winds at Syowa (69° S, 39° E), Antarctica: A comparison with simultaneous spaced antenna winds, J. Geophys. Res.-Atmos., 110, D24111, https://doi.org/10.1029/2005JD005849, 2005.

von Zahn, U., von Cossart, G., Fiedler, J., Fricke, K. H., Nelke, G., Baumgarten, G., Rees, D., Hauchecorne, A., and Adolfsen, K.: The ALOMAR Rayleigh/Mie/Raman lidar: objectives, configuration, and performance, Ann. Geophys., 18, 815–833, https://doi.org/10.1007/s00585-000-0815-2, 2000.

Wang, J., Zhou, J., Zang, H., Zhu, X., and Chen, W.: Conductively cooled 250-Hz single-frequency Nd laser, Chin. Opt. Lett., 8, 670–672, https://doi.org/10.3788/COL20100807.0670, 2010.

Yan, Z., Hu, X., Guo, W., Guo, S., Cheng, Y., Gong, J., and Yue, J.: Development of a mobile Doppler lidar system for wind and temperature measurements at 30–70 km, J. Quant. Spectrosc. Ra., 188, 52–59, https://doi.org/10.1016/j.jqsrt.2016.04.024, 2017.

Yang, B., Bu, L., Huang, C., Tan, Z., Hu, Z., Shu, S., Deng, C., Li, B., Ding, J., Yu, G., Wang, Y., Wang, C., Lin, W., and Zong, W.: High-precision Rayleigh Doppler lidar with fiber solid-state cascade-amplified high-power single-frequency laser for wind measurement, Remote Sens., 17, 573, https://doi.org/10.3390/rs17040573, 2025.